

1   **Changing available energy for extratropical cyclones and associated convection in Northern**  
2   **Hemisphere summer**

3   (short title: *Changing energy for extratropical cyclones*)

4   Charles G. Gertler<sup>1,\*</sup>, Paul A. O'Gorman<sup>1</sup>

5

6   <sup>1</sup>Department of Earth, Atmospheric and Planetary Sciences, Massachusetts Institute of  
7   Technology, 77 Massachusetts Avenue, Cambridge, Massachusetts 02139, USA

8

9   \*Corresponding Author. *Email:* [cgertler@mit.edu](mailto:cgertler@mit.edu)

10 **Abstract**

11 The circulation of the Northern Hemisphere extratropical troposphere has changed over recent  
12 decades, with marked decreases in extratropical cyclone activity and eddy kinetic energy (EKE)  
13 in summer and increases in the fraction of precipitation that is convective in all seasons.  
14 Decreasing EKE in summer is partly explained by a weakening meridional temperature gradient,  
15 but changes in vertical temperature gradients and increasing moisture also affect the mean  
16 available potential energy (MAPE), which is the energetic reservoir from which extratropical  
17 cyclones draw. Furthermore, the relation of changes in mean thermal structure and moisture to  
18 changes in convection associated with extratropical cyclones is poorly understood. Here we  
19 calculate trends in MAPE for the Northern extratropics in summer over the years 1979-2017,  
20 and we decompose MAPE into both convective and non-convective components. Non-  
21 convective MAPE decreased over this period, consistent with decreases in EKE and extratropical  
22 cyclone activity, but convective MAPE increased, implying an increase in the energy available to  
23 convection. Calculations with idealized atmospheres indicate that non-convective and  
24 convective MAPE both increase with increasing mean surface temperature and decrease with  
25 decreasing meridional surface temperature gradient, but convective MAPE is relatively more  
26 sensitive to the increase in mean surface temperature. These results connect changes in the  
27 atmospheric mean state with changes in both large-scale and convective circulations, and they  
28 suggest that extratropical cyclones can weaken even as their associated convection becomes  
29 more energetic.

30

31 **Keywords:** climate change; available energy; extratropical cyclones; convection; temperature  
32 trends; humidity trends

33 **Significance statement**

34 Extratropical cyclones and their associated convection play a central role in the weather of the  
35 midlatitudes and are changing with global warming. By analyzing trends in the energy of the  
36 mean state of the atmosphere that is available to be converted to kinetic energy, we show how  
37 the warming and moistening of the Northern Hemisphere extratropics relates to the observed  
38 weakening of extratropical summer cyclones. We also show that the component of this energy  
39 that can be released through convection has increased, despite the weakening of extratropical  
40 cyclones. Our results provide a unified framework that illustrates how the observed weakening  
41 of the extratropical cyclones in summer can occur while at the same time convection becomes  
42 more energetic.

43

44 **Author contributions**

45 C.G.G. performed the analyses and produced all figures. C.G.G. and P.A.O'G. contributed to  
46 interpretation of the results and to writing the manuscript.

47

48 \body

49 **Introduction**

50 Distinct patterns of change have emerged in the thermal structure and moisture content  
51 of the Northern Hemisphere extratropical troposphere (1-4), as seen from homogenized  
52 radiosonde data (see Methods) for the summer season in Fig. 1. Notably, the meridional

53 temperature gradient has weakened in the lower- and middle-troposphere (Fig. 1a), and the  
54 troposphere has experienced a general moistening (Fig. 1b). The weakening of the meridional  
55 temperature gradient is thought to contribute to the observed weakening of EKE and cyclone  
56 activity levels (5, 6), with implications for regional climate and air quality (7). However, eddy  
57 behavior is also affected by changes in moisture content and static stability. For example,  
58 amplified low-level warming (Fig. 1a), which is more clearly evident in reanalysis trends that  
59 extend to the surface (Fig. S1a), implies decreased static stability in the lower troposphere,  
60 which together with increasing specific humidity (Fig. 1b) would tend to increase the growth  
61 rates of eddies, opposing the weakening effect from the meridional temperature gradients.  
62 Projections of 21<sup>st</sup> century climate change with coupled climate models also show a decrease in  
63 EKE in the Northern Hemisphere in summer that has been linked to weakening lower-  
64 tropospheric meridional temperature gradients (8) and increases in extratropical static stability  
65 that occurs in the projections in this season (9). The changes in mean thermal structure and  
66 moisture could also cause changes in the energy available to convection; large increases in the  
67 convective fraction of precipitation have been observed for all seasons over Eurasia (10), and  
68 there is some evidence for increases in convective available potential energy (CAPE) as the  
69 climate has warmed (11). However, CAPE is calculated from instantaneous vertical profiles of  
70 temperature and humidity and cannot be directly related to changes in mean temperature and  
71 moisture in the extratropics.

72 Mean available potential energy (MAPE) provides a useful framework with which to  
73 connect the mean thermal structure (including both meridional temperature gradients and  
74 static stability) and moisture content of the extratropical atmosphere to EKE and, as discussed

75 below, to available energy for convection. MAPE is defined as the difference in enthalpy  
76 between an atmosphere's mean state and the minimum-enthalpy state possible from  
77 reversible, adiabatic parcel rearrangements (12). MAPE may be calculated neglecting latent  
78 heating (dry MAPE) (12) or taking it into account (moist MAPE) (13, 14). EKE scales linearly with  
79 dry and moist MAPE in extratropical, baroclinic environments in a wide range of idealized  
80 climate model experiments (15-17). A recent study (18) that imposed isolated thermal forcings  
81 at different latitudes and levels found that the scaling of EKE with MAPE can break down in  
82 some cases, but that it generally performs better than considering the change in meridional  
83 temperature gradient or static stability alone. Importantly, EKE also scales linearly with MAPE  
84 over the seasonal cycle in the extratropics in both hemispheres based on reanalysis data, and  
85 under climate change in coupled model projections, including for intermodel differences (9).

86 Here, we calculate changes in moist MAPE over recent decades and use the results to  
87 better understand observed changes in the circulation. Some recent studies suggest an  
88 increasing trend in global eddy energy, but these changes are dominated by the Southern  
89 Hemisphere and their magnitude is dataset-dependent (19, 20). We focus on the Northern  
90 Hemisphere extratropics in June-July-August (JJA), given the clear reported trends in cyclonic  
91 activity (5, 6) and convective precipitation fraction (10) in that season and hemisphere. Using  
92 moist rather than dry MAPE allows us to consider the role of latent heating and the implications  
93 for moist convection.

94

95 **Mean available potential energy (MAPE)**

96            We use zonal- and seasonal-mean temperatures and humidities from the ERA-Interim  
97    Reanalysis (21) to calculate MAPE for JJA and the latitude band 20-80N over the years 1979-  
98    2017. ERA-Interim provides complete spatial and temporal coverage, and trends in mean  
99    temperature from ERA-Interim are similar to those from homogenized radiosonde data when  
100    subsampled to that data (compare Fig. 1a and Fig. S2a). However, the subsampled humidity  
101    trends do not agree well with a homogenized radiosonde humidity data (compare Fig. 1b and  
102    Fig. S3b), and this issue with ERA-Interim relative humidity trends could partly relate to the use  
103    of unhomogenized radiosonde humidities as input to the reanalysis (4). To avoid this bias in  
104    humidity trends, we hold relative humidity constant in time using its climatological values from  
105    ERA-Interim. This gives mean specific humidity trends that are more consistent with the  
106    radiosonde data (Fig. S2b; see Methods for details).

107            The air-parcel rearrangement in the calculation of moist MAPE for JJA is illustrated in  
108    Fig. 2a based on climatological temperatures and humidities. The general pattern is of rising air  
109    originating at lower latitudes and sinking air originating at higher latitudes, corresponding to  
110    large-scale slantwise motion in baroclinic eddies in the atmosphere. In addition, there is a  
111    substantial air mass (highlighted in blue in Fig. 2a) that moves from the boundary layer to the  
112    upper troposphere and which is bounded by a discontinuity in the mapping of the parcel  
113    rearrangement. The ascent of this air mass to the upper troposphere results in a vertical  
114    reordering of air parcels originating at low latitudes which we interpret as corresponding to  
115    deep convection in the atmosphere. While the air mass originates at low latitudes, its ascent  
116    can occur in the midlatitudes, since extratropical cyclones advect air poleward before deep  
117    ascent occurs (22, 23). The parcel rearrangement for winter (Fig. S4a) also shows deep ascent

118 but with a weaker signature of convection and no discontinuity, consistent with deep ascent in  
119 winter predominantly occurring as slow ascent in warm conveyor belts rather than rapid deep  
120 convection, as seen in recent high-resolution simulations (23).

121 Following previous work (9), we also calculate non-convective MAPE which allows for  
122 latent heating but does not allow for release of convective instability as represented by vertical  
123 reordering of air originating at a given latitude (Fig 2b; see Methods). We expect EKE to scale  
124 with non-convective MAPE rather than the full moist MAPE because release of convective  
125 instability involves local dissipation of kinetic energy without necessarily contributing to large-  
126 scale EKE, and because convection is associated with mixing and diffusion of water vapor which  
127 acts as a sink of moist MAPE (24).

128 Non-convective MAPE is always less than or equal to moist MAPE (9), and here we  
129 introduce the concept of convective MAPE, defined as the moist MAPE minus non-convective  
130 MAPE. Convective MAPE provides a link between convection and the mean state of the  
131 atmosphere, in contrast to CAPE which must be calculated from instantaneous soundings.  
132 Conditional instability of the mean state of the atmosphere is limited to low latitudes and does  
133 not contribute strongly to convective MAPE (see Methods), and thus convective MAPE must be  
134 primarily generated by the large-scale circulation driven by the meridional temperature  
135 gradient. The weak conditional instability of the mean state of the atmosphere also implies  
136 that the alternative approach of calculating moist MAPE at each latitude in isolation (without  
137 allowing meridional movement) and then averaging in latitude would give a much smaller value  
138 than the convective MAPE.

139 Convective MAPE is calculated using adiabatic rearrangements, and therefore it does  
140 not account for convective instability driven by surface fluxes or radiative cooling. We interpret  
141 convective MAPE as the energy available for moist convection driven by large-scale ascent in  
142 extratropical cyclones, and our study of changes in convective MAPE is complementary to  
143 previous studies that have investigated the physical basis of changes in tropical CAPE (25-27)  
144 and changes in midlatitude extreme CAPE driven by surface fluxes over land (28).

145

#### 146 **Changing energetic reservoirs**

147 Time series and trends in MAPE for JJA over 20-80N and 1979-2017 are shown in Fig. 3.  
148 Non-convective MAPE demonstrates a downward trend of -1.5% per decade, with a 90%  
149 confidence interval of [-2.8, -0.3] % per decade, consistent in terms of percentage change with  
150 the downward trend in EKE (also calculated from ERA-Interim data) of -1.3% per decade, as  
151 seen in Fig. 3a. Therefore, changes in mean temperature and humidity, combined into non-  
152 convective MAPE, are sufficient to explain the sign and magnitude of the change in EKE. The  
153 trends in dry and moist MAPE are also downward and the trend of dry MAPE is similar in  
154 magnitude to that of non-convective MAPE (Fig. S5b and Fig. S5e).

155 Interestingly, EKE and non-convective MAPE are not positively correlated for year-to-  
156 year variability when the timeseries in Fig. 3a are detrended. This different behavior for year-to-  
157 year variability as compared to longer-term trends is likely because EKE and MAPE have a  
158 different relationship for unforced variability as compared to forced variability. For forced  
159 variability, such as the seasonal cycle of the storm tracks or the response of the storm tracks to  
160 climate change, an increase in EKE is associated with an increase in MAPE (9). For unforced

161 variability of the storm tracks, an increase in EKE is associated with amplified heat fluxes which  
162 lead to a subsequent decrease in baroclinicity and MAPE (29-31).

163 In contrast to the decreasing trend in non-convective MAPE, convective MAPE  
164 demonstrates an upward trend of  $1.1 \text{ J kg}^{-1}$  per decade, with a 90% confidence interval of [0.7,  
165  $1.7] \text{ J kg}^{-1}$  per decade (Fig. 3b). This increase in the energy available to moist convection  
166 associated with extratropical cyclones implies a tendency toward more convective precipitation  
167 in summer in midlatitudes. Observations show a robust increase in the convective fraction of  
168 precipitation over Northern Eurasia (10), and it would be interesting to study changes in the  
169 convective fraction of precipitation in other midlatitude regions.

170 The signs and magnitudes of the trends in non-convective and convective MAPE and in  
171 EKE are similar for narrower (30-70N) and wider (10-90N) latitude bands (Fig. S5). We report  
172 the absolute rather than percentage changes in convective MAPE because the absolute changes  
173 are less sensitive to the latitude band chosen. Absolute values for all types of MAPE are shown  
174 in Fig. S6.

175

#### 176 **Relation to surface temperatures in idealized atmospheres**

177 To better understand how climate change can cause changes of opposite sign in non-  
178 convective MAPE and convective MAPE, we next consider how changes in mean surface  
179 temperature and meridional surface temperature gradient affect these energetic reservoirs in  
180 idealized atmospheres that are representative of Northern Hemisphere summer. We prescribe  
181 simple meridional profiles of surface temperature and vary the mean surface temperature and  
182 meridional surface temperature gradient independently. Given that the middle and lower

183 troposphere are frequently close to neutral to moist convection in summer in the Northern  
184 extratropics (32), we construct vertical temperature profiles in idealized atmospheres with  
185 prescribed relative humidity such that the virtual temperatures in the troposphere match the  
186 virtual temperatures in a reversible moist adiabat of a parcel lifted from the surface (see  
187 Methods for details). By this construction each individual column in isolation is not conditionally  
188 unstable and has no available potential energy, and thus non-zero convective MAPE must arise  
189 because of the meridional temperature gradient and the resulting lateral and vertical motion.

190 Fig. 4 shows the variations in MAPE as a function of mean surface temperature and the  
191 mean meridional surface temperature gradient over 20-80N in the idealized atmospheres. The  
192 ranges shown are roughly centered on the ERA-Interim mean temperatures and temperature  
193 gradients for Northern Hemisphere JJA of 292 K and 0.44 K degree<sup>-1</sup>. Based on the ERA-Interim  
194 trends for JJA, we find that surface temperature increased by roughly 1 K and the surface  
195 meridional temperature gradient decreased by roughly 0.02 K degree<sup>-1</sup> over the whole period  
196 (Fig. S7), and the observed changes in this time period are indicated by the red arrows in Fig. 4.  
197 Non-convective MAPE increases with the meridional temperature gradient as would be  
198 expected given that it behaves similarly to dry MAPE, which increases as the meridional  
199 temperature gradient squared with some compensation from increases in static stability (33).  
200 Non-convective MAPE also increases with mean surface temperature which likely reflects both  
201 increases in latent heating and induced changes in meridional temperature gradients aloft. On  
202 the other hand, convective MAPE has two different behavior regimes. For very weak meridional  
203 temperature gradients and thus weak large-scale overturning circulation, convective MAPE  
204 primarily increases with the meridional temperature gradient because the amount of air that

205 reaches saturation increases with the strength of ascent at lower latitudes. For stronger  
206 meridional temperature gradients and thus stronger large-scale overturning, convective MAPE  
207 is more strongly a function of mean temperature, and this is the regime in which the observed  
208 JJA parameters fall. To understand why convective MAPE is sensitive to mean temperature, we  
209 first note that the vertical gradient in potential temperature along a moist adiabat increases  
210 with surface temperature (34), which implies that the ability of a given amount of large-scale  
211 ascent to cool the free troposphere and destabilize the column will also increase with  
212 temperature. The additional dependence on meridional temperature gradient reflects the  
213 ability of stronger temperature gradients to drive more ascent. The idealized atmosphere  
214 results show that convective MAPE is relatively more sensitive to mean surface temperature as  
215 compared to non-convective MAPE, and this helps explain why convective MAPE can increase  
216 in response to mean warming and a weakening meridional temperature gradient even though  
217 non-convective MAPE decreases.

218

219 **Discussion**

220 Our results show that there have been opposite-signed changes in the energy available  
221 to the large-scale circulations and associated moist convection in recent decades in Northern  
222 extratropical summer, and that these changes are consistent with decreases in eddy kinetic  
223 energy and also consistent in sign with observed increases in the convective precipitation  
224 fraction. The changes in MAPE thus serve as a bridge between changes in the mean  
225 temperature and moisture of the atmosphere and changes in extratropical circulations. The  
226 MAPE framework may also be useful for considering past climate states based on surface

227 temperature proxies to the extent that we can assume a vertical stratification in Northern  
228 midlatitude summer that is close to moist adiabatic.

229 While the link between changes in MAPE and EKE has been extensively studied in  
230 previous studies (15-18), our results suggest a need for more investigation into connections  
231 between the mean state of the extratropical atmosphere (including both mean temperature  
232 and temperature gradients) and its convective behavior. For example, future work could  
233 compare convective MAPE with other measures of convection, such as instantaneous CAPE and  
234 the convective fraction of precipitation, across the seasonal cycle, in idealized simulations, and  
235 in warming scenarios. It is also important to investigate the contribution of zonal asymmetries  
236 to trends in non-convective and convective MAPE since these asymmetries are not included in  
237 the zonal-mean MAPE considered here.

238 Decreasing non-convective MAPE and increasing convective MAPE are consistent with  
239 model projections for Northern midlatitude summer over the 21st century (9). However, the  
240 large decrease of roughly 6% in non-convective MAPE found here over recent decades is of  
241 similar magnitude to the multimodel-mean projected decrease in non-convective MAPE over  
242 the whole 21st century - a finding consistent with the observed decrease in cyclone activity  
243 being near the extreme end of what different climate models simulate for recent decades (6).  
244 Substantial components of regional Arctic amplification may result from unforced variability,  
245 for example as a result of the Atlantic Multi-decadal Oscillation (35) or via teleconnection to  
246 tropical Pacific variability (36), and future work could also investigate the contributions of  
247 anthropogenic forcing versus unforced variability to trends in MAPE.

248

249

250 **Methods**

251 *Trends*

252 All trends of time series are calculated using the Theil-Sen estimator, and 90% confidence  
253 intervals are calculated using the bootstrapping percentile method. Zonal average trends in  
254 temperature and humidity from radiosonde datasets, and reanalysis products subsampled to  
255 radiosonde locations, are calculated as follows: stations are binned in 10° latitude bands, and  
256 the trend for each pressure level and latitude band is determined as the median trend of the  
257 seasonal average at that pressure level among the stations in that latitude band. The use of the  
258 median trend in latitude bands limits the influence of outlier trends in the radiosonde data (3).

259

260 *Temperature and humidity data*

261 For the calculation of MAPE, monthly mean temperature and humidity data from 1979-2017  
262 with a grid resolution of 2.5° by 2.5° are taken from the ERA-Interim dataset, a global  
263 atmospheric reanalysis produced by the European Centre for Medium-Range Weather  
264 Forecasts (ECMWF) (21). Seasonal-mean temperature and humidity are first calculated at each  
265 gridpoint. The zonal mean is then taken for a given year excluding any gridpoints at which the  
266 monthly pressure is greater than the monthly surface pressure at that point by more than 25  
267 hPa (the pressure spacing near the surface) for any of the months in the season. The mean  
268 surface temperatures and surface meridional temperature gradients shown in Fig. S7 are  
269 calculated from the zonal and seasonal mean of the 1000hPa temperatures at each latitude as  
270 calculated above, and then meridionally averaged with area weighting.

271           Observational temperature data are taken from IUKv2 (3), a radiosonde dataset  
272           homogenized by Iterative Universal Kriging to correct for time-varying instrument biases. For  
273           direct comparison with IUKv2, ERA-Interim data are subsampled in space and time to the  
274           coordinates closest to the station data in the IUKv2 dataset and trends are calculated as  
275           described above. We chose ERA-Interim for use in this paper because of its relatively good  
276           agreement with the radiosonde data in terms of temperature trends when subsampled to the  
277           station locations (compare Fig. 1a with Fig. S2a), whereas other reanalysis products that we  
278           analyzed were found to have less good agreement, resulting in MAPE trends different to those  
279           presented here, including differences of sign in some cases.

280           Observational specific humidity data are taken from the homoRS92 dataset, a  
281           homogenized global, twice-daily humidity dataset that consists of the dataset described in ref.  
282           4, supplemented with dry-bias corrected data from Vaisala RS92 soundings (37). In reporting  
283           relative humidity and specific humidity, this dataset employs a separate homogenized air  
284           temperature radiosonde product (38) combined with the homogenized dewpoint depression.  
285           Due to missing data in this dataset (which unlike IUKv2 is not iteratively filled), the following  
286           processing procedure is applied when determining trends: [1] at individual stations and  
287           pressure levels, only days with two measurements are considered, [2] only months with at least  
288           70% of days are considered, [3] only JJA averages with all three months present are considered,  
289           and [4] only trends based on at least 70% of years are considered. The zonal-median trend  
290           following this procedure is shown in Fig. 1b. Trends in ERA-Interim specific humidity data are  
291           compared to the observations by subsampling to the homoRS92 dataset station locations.  
292           Comparing the radiosonde humidity trends (Fig. 1b) to the subsampled ERA-Interim humidity

293 trends (Fig. S3b) reveals a large discrepancy with much too weak moistening in ERA-Interim. To  
294 avoid this bias, we instead use the climatological JJA-mean relative humidity from ERA-Interim  
295 (averaged over 1979-2017) as the humidity input to the JJA MAPE calculation for a given year.  
296 This approach is consistent with expectations of small trends in relative humidity in the  
297 troposphere (39), and it implies trends in specific humidity that are more consistent with the  
298 homogenized radiosonde trends in specific humidity (compare Fig. 1b and Fig. S2b). In  
299 calculating the JJA specific humidities for Fig. S2b and in our calculations of MAPE, we use the  
300 saturation vapor pressure formulae over ice and liquid described in Simmons et al. (1999) (40)  
301 but with the ice and liquid phases merged using the method described in Wang and Randall  
302 (1994) (41). The same saturation vapor pressure formulation is also used in calculating the  
303 moist adiabats in the idealized atmospheres (see below).

304

#### 305 *MAPE calculations*

306 The moist MAPE and its components are calculated for each year using the zonal- and JJA-mean  
307 temperatures and relative humidities from ERA-Interim. The temperature for a given year is the  
308 JJA-mean temperature for that year. As discussed above, the relative humidity is the  
309 climatological (1979-2017) JJA-mean relative humidity. Performing MAPE calculations using  
310 time-varying relative humidity (instead of climatological values) from ERA-Interim results in  
311 qualitatively similar results (Fig. S8), but the increase in convective MAPE is  $0.6 \text{ J kg}^{-1}$  per decade  
312 (Fig. S8b), which is roughly half the rate of increase that constant relative humidity implies. The  
313 zonal-mean temperatures and relative humidities for each JJA are first interpolated to a 40 by  
314 40 equal-area staggered grid (13) in order to convert a 2D problem in pressure and latitude

315 coordinates into a 1D problem in pressure coordinates only, although the original latitude for  
316 each parcel is stored for use in the calculation of non-convective MAPE.

317 To calculate moist MAPE, we use the divide-and-conquer algorithm (14), which is a  
318 recursive algorithm that builds a low-enthalpy reference state by dividing the atmospheric  
319 domain into smaller subdomains. At each division, the pressure-derivative of enthalpy is  
320 evaluated at the mid-pressure of the subdomain and used to order the parcels from top to  
321 bottom of the subdomain; the top and bottom halves are then assigned to new subdomains.

322 The divide-and-conquer algorithm has been found to work well in practice (14, 42), and in  
323 particular it gives a moist MAPE that is almost identical to that calculated using the exact  
324 Munkres algorithm for a similar case to the one considered here (14). We use divide and  
325 conquer rather than Munkres because divide and conquer is faster and more straightforward to  
326 adapt to calculate convective and non-convective MAPE.

327 To calculate non-convective MAPE (9), the divide-and-conquer algorithm is modified  
328 such that when sorting parcels from top to bottom in a subdomain, parcels from a given initial  
329 latitude may not change their vertical ordering (i.e. whether one parcel is above the other). This  
330 condition that parcels cannot “leapfrog” in pressure over other parcels from the same initial  
331 latitude leads to the continuous remapping of parcel pressure shown in Fig. 2b, in which the  
332 reference pressure (the pressure in the minimum-enthalpy state) is a monotonic function of  
333 pressure at a given latitude.

334 To calculate convective MAPE, we simply subtract the non-convective MAPE from the  
335 moist MAPE. The magnitude of convective MAPE is reported per unit mass of the entire  
336 atmosphere in the specified latitude band (rather than the mass of a lifted parcel as is the case

337 for CAPE), and as a result the reported values are much smaller than typical CAPE values in  
338 convective conditions. For JJA and 20-80N, the mass of the lifted air in the moist MAPE  
339 calculation (the blue shaded region in Fig.2a) is roughly 6% of the mass of the atmosphere over  
340 20-80N, and the value of convective MAPE of roughly  $32 \text{ J kg}^{-1}$  becomes  $530 \text{ J kg}^{-1}$  when  
341 normalized by the mass of lifted air, which is comparable to typical CAPE values. Convective  
342 MAPE should not be confused with generalized CAPE (GCAPE) which is the moist available  
343 potential energy of a column of air in isolation (41, 43). The moist available potential energy of  
344 the climatological and zonal mean at each latitude in isolation is only non-zero equatorward of  
345 30N, and its meridional average with area weighting over 20-80N is only  $1.3 \text{ J kg}^{-1}$  as compared  
346 to convective MAPE of  $32 \text{ J kg}^{-1}$  for the same latitude band. Thus, conditional instability of the  
347 mean state does not contribute strongly to convective MAPE.

348 To calculate dry MAPE, the divide-and-conquer algorithm is used as for the moist MAPE  
349 calculation but with the input relative humidity set to zero.

350

351 *EKE Calculations*

352 To calculate EKE, we first apply a 2.5-6 day Butterworth bandpass filter to 4-times daily  
353 horizontal winds on a  $2.5^\circ$  by  $2.5^\circ$  grid from ERA-Interim reanalysis over 1979-2017. Data below  
354 the surface pressure are removed (we do not use the approach described above for the monthly  
355 temperature and humidity because here we are using instantaneous data). A mass-weighted  
356 vertical integral of kinetic energy of the filtered wind time series is calculated at each latitude-  
357 longitude grid point to give the local vertically integrated EKE. A JJA- and area-weighted mean

358 of the EKE is then calculated to give the time and spatial mean EKE over the specified latitude  
359 band for a given year.

360

361 *Idealized Atmospheres*

362 Idealized atmospheres are constructed by first imposing profiles of surface air temperature,  $T_s$ ,  
363 as a function of latitude,  $\phi$ :

364

365 
$$T_s(\phi) = T_{eq} - \Delta_T \sin^2 \phi,$$

366

367 where  $T_{eq}$  is the surface temperature at the equator and  $\Delta_T$  is a parameter controlling the  
368 meridional surface temperature gradient. Vertical temperature profiles in the atmosphere  
369 based on the surface temperatures are then determined as follows. First, reversible moist  
370 adiabatic parcel ascents with an assumed initial surface relative humidity of 85% are  
371 constructed in which the temperature profile follows a dry adiabat until saturation, after which  
372 it follows a saturated moist adiabat. A stratosphere with a constant temperature of 240K is  
373 imposed above the tropopause, with the tropopause defined as the level at which the parcel  
374 ascents reach 240K. While warmer than the real tropopause, this choice limits the extent to  
375 which upper-level meridional temperature gradients become much steeper than in the real  
376 atmosphere, inflating MAPE values. Next, vertical relative humidity profiles are imposed with  
377 boundary-layer relative humidity of 85% from the surface up to 900 hPa, free-tropospheric  
378 relative humidity of 45% between 900 hPa and the tropopause, and stratospheric relative  
379 humidity of 0.01%. Using one value of free-tropospheric relative humidity at all latitudes is a

380 simplification, and we chose a value close to the climatological value at lower latitudes where  
381 ascending air originates. Lastly, temperature profiles are constructed such that the virtual  
382 temperature profile with the imposed relative humidity values matches the virtual temperature  
383 profile of the moist adiabat. This procedure allows us to produce a sub-saturated atmosphere  
384 that is neutral to moist convective instability. As a result, the convective MAPE is driven by the  
385 large-scale pattern of ascent and descent rather than having a contribution from conditional  
386 instability in the initial condition at a given latitude. In particular, the moist available potential  
387 energy of a column of air at a given latitude in isolation, the GCAPE (43), is zero.

388 We solve for  $T_{eq}$  and  $\Delta_T$  to produce an evenly spaced grid of mean surface  
389 temperatures and surface temperature gradients averaged with area weighting over the  
390 latitude band 20-80N. The mean surface temperatures are 289-295 K at increments of 0.5 K,  
391 and the mean meridional surface temperature gradients are 0.15-0.65 K degree<sup>-1</sup> at increments  
392 of 0.05 K degree<sup>-1</sup>. The moist MAPE and non-convective and convective components are  
393 calculated for each of these idealized atmospheres over 20-80N. The resulting values of moist  
394 MAPE and its convective and non-convective components are shown in Fig. 4.

395 Based on ERA-Interim over JJA and 20-80N, the mean surface temperature is 292 K and  
396 the mean meridional surface temperature gradient is 0.44 K degree<sup>-1</sup> (Fig. S7). At these values,  
397 the non-convective MAPE for the idealized atmosphere is 325 J kg<sup>-1</sup> as compared to 185 J kg<sup>-1</sup>  
398 from ERA-Interim, and the convective MAPE for the idealized atmosphere is 9 J kg<sup>-1</sup> as  
399 compared to 32 J kg<sup>-1</sup> from ERA-Interim. The larger non-convective MAPE in the idealized  
400 atmosphere likely relates to the meridional temperature gradients aloft being too steep  
401 because the idealization of moist-adiabatic lapse rates becomes less accurate at higher

402 latitudes. The smaller convective MAPE in the idealized atmosphere may relate to inaccuracy in  
403 the idealized relative humidity structure since convective MAPE only receives a small  
404 contribution from conditional instability of the mean state in ERA-Interim. However, these  
405 discrepancies in absolute values are not problematic because our aim in using the idealized  
406 atmosphere is to better understand the relative changes in convective and non-convective  
407 MAPE as a function of the surface parameters.

408

#### 409 **Acknowledgements**

410 We thank three anonymous reviewers for valuable comments. C.G.G. acknowledges support  
411 from the National Science Foundation Graduate Research Fellowship Program under NSF Grant  
412 Number 1122374. P.A.O'G. acknowledges support from NSF AGS 1552195 and NSF AGS  
413 1749986. We are grateful to T. Cronin, H. Wernli, E. Chang and S. Schemm for helpful  
414 discussions, to A. Dai and J. Huang for use of the homoRS92 Dataset, to S. Sherwood for use of  
415 the IUK2 dataset, and to the European Center for Medium-Range Weather Forecasts for use of  
416 the ERA-Interim reanalysis.

417

#### 418 **References**

419

420 1. Screen JA & Simmonds I (2010) The central role of diminishing sea ice in recent Arctic  
421 temperature amplification. *Nature* 464:1334-1337.

422 2. McCarthy MP, Thorne PW, & Titchner HA (2009) An analysis of tropospheric humidity  
423 trends from radiosondes. *J Clim* 22:5820-5838.

424 3. Sherwood SC & Nishant N (2015) Atmospheric changes through 2012 as shown by  
425 iteratively homogenized radiosonde temperature and wind data (IUKv2). *Environ Res*  
426 *Lett* 10:054007.

427 4. Dai A, *et al.* (2011) A new approach to homogenize daily radiosonde humidity data. *J*  
428 *Clim* 24:965-991.

429 5. Coumou D, Lehmann J, & Beckmann J (2015) The weakening summer circulation in the  
430 Northern Hemisphere mid-latitudes. *Science* 348:324-327.

431 6. Chang EKM, Ma CG, Zheng C, & Yau AMW (2016) Observed and projected decrease in  
432 Northern Hemisphere extratropical cyclone activity in summer and its impacts on  
433 maximum temperature. *Geophys Res Lett* 43:2200-2208.

434 7. Leibensperger EM, Mickley LJ, & Jacob DJ (2008) Sensitivity of US air quality to mid-  
435 latitude cyclone frequency and implications of 1980-2006 climate change. *Atmos Chem  
436 Phys* 8:7075-7086.

437 8. Harvey BJ, Shaffrey LC, & Woollings TJ (2014) Equator-to-pole temperature differences  
438 and the extra-tropical storm track responses of the CMIP5 climate models. *Clim Dyn*  
439 43:1171-1182.

440 9. O'Gorman PA (2010) Understanding the varied response of the extratropical storm  
441 tracks to climate change. *Proc Natl Acad Sci U S A* 107:19176-19180.

442 10. Ye H, Fetzer EJ, Wong S, & Lambrightsen BH (2017) Rapid decadal convective  
443 precipitation increase over Eurasia during the last three decades of the 20th century. *Sci  
444 Adv* 3:e1600944

445 11. Riemann-Campe K, Fraedrich K, & Lunkeit F (2009) Global climatology of Convective  
446 Available Potential Energy (CAPE) and Convective Inhibition (CIN) in ERA-40 reanalysis.  
447 *Atmos Res* 93:534-545.

448 12. Lorenz EN (1955) Available potential energy and the maintenance of the general  
449 circulation. *Tellus* 7:157-167.

450 13. Lorenz EN (1979) Numerical evaluation of moist available energy. *Tellus* 31:230-235.

451 14. Stansifer EM, O'Gorman PA, & Holt JI (2017) Accurate computation of moist available  
452 potential energy with the Munkres algorithm. *Q J R Meteorol Soc* 143:288-292.

453 15. Schneider T & Walker CC (2008) Scaling laws and regime transitions of macroturbulence  
454 in dry atmospheres. *J Atmos Sci* 65:2153-2173.

455 16. O'Gorman PA & Schneider T (2008) Energy of midlatitude transient eddies in idealized  
456 simulations of changed climates. *J Clim* 21:5797-5806.

457 17. O'Gorman PA (2011) The effective static stability experienced by eddies in a moist  
458 atmosphere. *J Atmos Sci* 68:75-90.

459 18. Yuval J & Kaspi Y (2017) The effect of vertical baroclinicity concentration on atmospheric  
460 macroturbulence scaling relations. *J Atmos Sci* 74:1651-1667.

461 19. Pan Y, *et al.* (2017) Earth's changing global atmospheric energy cycle in response to  
462 climate change. *Nat Commun* 8:14367.

463 20. Kim W & Choi Y-S (2017) Long-term change of the atmospheric energy cycles and  
464 weather disturbances. *Clim Dyn* 49:3605-3617.

465 21. Dee DP, *et al.* (2011) The ERA-Interim reanalysis: configuration and performance of the  
466 data assimilation system. *Q J R Meteorol Soc* 137:553-597.

467 22. Madonna E, Wernli H, Joos H, & Martius O (2014) Warm conveyor belts in the ERA-  
468 Interim dataset (1979-2010). Part I: climatology and potential vorticity evolution. *J Clim*  
469 27:3-26.

470 23. Rasp S, Selz T, & Craig GC (2016) Convective and slantwise trajectory ascent in  
471 convection-permitting simulations of midlatitude cyclones. *Mon Weather Rev* 144:3961-  
472 3976.

473 24. Pauluis O (2007) Sources and sinks of available potential energy in a moist atmosphere. *J  
474 Atmos Sci* 64:2627-2641.

475 25. Seeley JT & Romps DM (2015) Why does tropical convective available potential energy  
476 (CAPE) increase with warming? *Geophys Res Lett* 42:10429-10437.

477 26. Singh MS, Kuang ZM, Maloney ED, Hannah WM, & Wolding BO (2017) Increasing  
478 potential for intense tropical and subtropical thunderstorms under global warming. *Proc  
479 Natl Acad Sci U S A* 114:11657-11662.

480 27. Singh MS & O'Gorman PA (2013) Influence of entrainment on the thermal stratification  
481 in simulations of radiative-convective equilibrium. *Geophys Res Lett* 40:4398-4403.

482 28. Agard V & Emanuel K (2017) Clausius-Clapeyron scaling of peak CAPE in continental  
483 convective storm environments. *J Atmos Sci* 74:3043-3054.

484 29. Thompson PD (1987) Large-scale dynamic response to differential heating: statistical  
485 equilibrium states and amplitude vacillation *J Atmos Sci* 44:1237-1248.

486 30. Ambaum MHP & Novak L (2014) A nonlinear oscillator describing storm track variability.  
487 *Q J R Meteorol Soc* 140:2680-2684.

488 31. Thompson DWJ & Barnes EA (2014) Periodic variability in the large-scale Southern  
489 Hemisphere atmospheric circulation. *Science* 343:641-645.

490 32. Korty RL & Schneider T (2007) A climatology of the tropospheric thermal stratification  
491 using saturation potential vorticity. *J Clim* 20:5977-5991.

492 33. Schneider EK (1981) On the amplitudes reached by baroclinically unstable disturbances.  
493 *J Atmos Sci* 38:2142-2149.

494 34. Betts AK & Harshvardhan (1987) Thermodynamic constraint on the cloud liquid water  
495 feedback in climate models. *J Geophys Res Atmos* 92:8483-8485.

496 35. Chylek P, Folland CK, Lesins G, Dubey MK, & Wang MY (2009) Arctic air temperature  
497 change amplification and the Atlantic Multidecadal Oscillation. *Geophys Res Lett*  
498 36:L14801.

499 36. Ding Q, *et al.* (2014) Tropical forcing of the recent rapid Arctic warming in northeastern  
500 Canada and Greenland. *Nature* 509:209-212.

501 37. Wang J, *et al.* (2013) Radiation dry bias correction of Vaisala RS92 humidity data and its  
502 impacts on historical radiosonde data. *J Atmos Ocean Technol* 30:197-214.

503 38. Haimberger L, Tavolato C, & Sperka S (2008) Toward elimination of the warm bias in  
504 historic radiosonde temperature records - Some new results from a comprehensive  
505 intercomparison of upper-air data. *J Clim* 21:4587-4606.

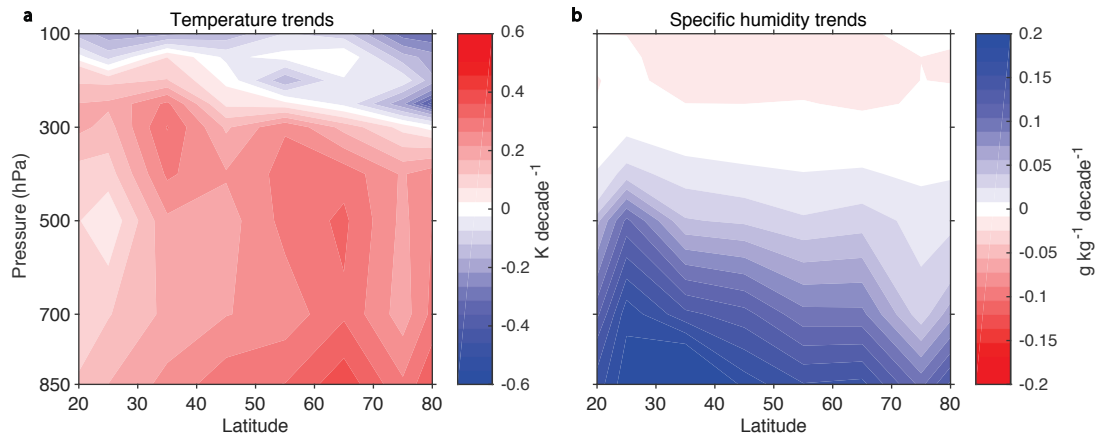
506 39. Sherwood SC, *et al.* (2010) Relative humidity changes in a warmer climate. *J Geophys  
507 Res Atmos* 115:D09104.

508 40. Simmons AJ, Untch A, Jakob C, Källberg P, & Undén P (1999) Stratospheric water vapour  
509 and tropical tropopause temperatures in ECMWF analyses and multi-year simulations. *Q  
510 J R Meteorol Soc* 125:353-386.

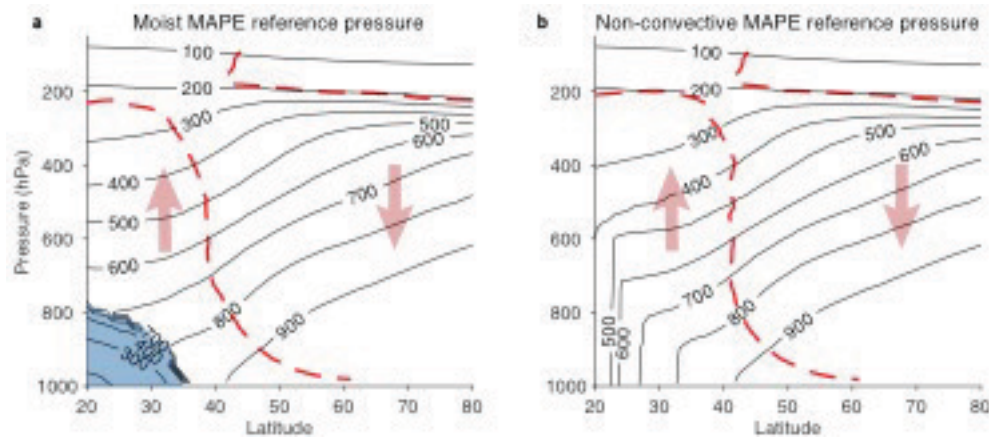
511 41. Wang J & Randall DA (1994) The moist available energy of a conditionally unstable  
512 atmosphere. Part II. Further analysis of GATE data. *J Atmos Sci* 51:703-710.

513 42. Harris BL & Tailleux R (2018) Assessment of algorithms for computing moist available  
514 potential energy. *Q J R Meteorol Soc* 144:1501-1510

515 43. Randall DA & Wang J (1992) The moist available energy of a conditionally unstable  
516 atmosphere. *J Atmos Sci* 49:240-255.

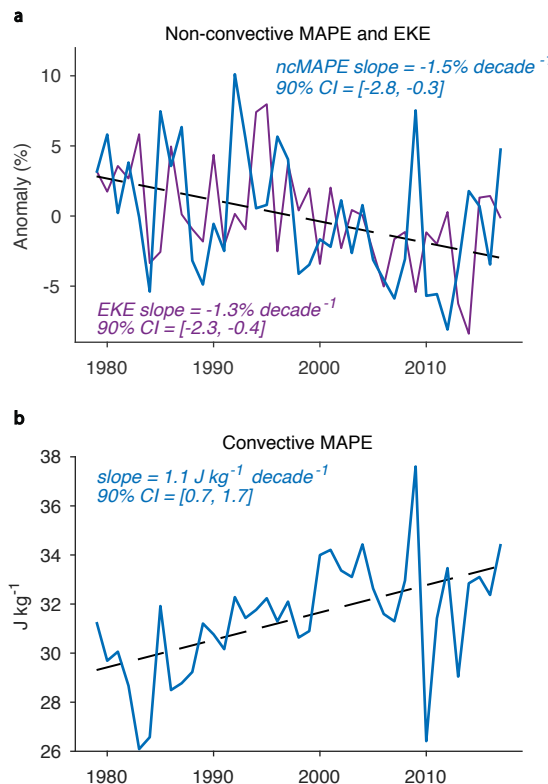


519 **Figure 1:** Observed changes in summer (JJA) temperature and moisture of the Northern  
 520 extratropics. (a) Median JJA temperature trend in 10-degree latitude bands from the IUKv2  
 521 radiosonde dataset (3) (1979-2015), and (b) median JJA specific humidity trend in 10-degree  
 522 latitude bands from the homoRS92 radiosonde dataset (4) (1979-2010). See Methods for  
 523 datasets and calculation details.



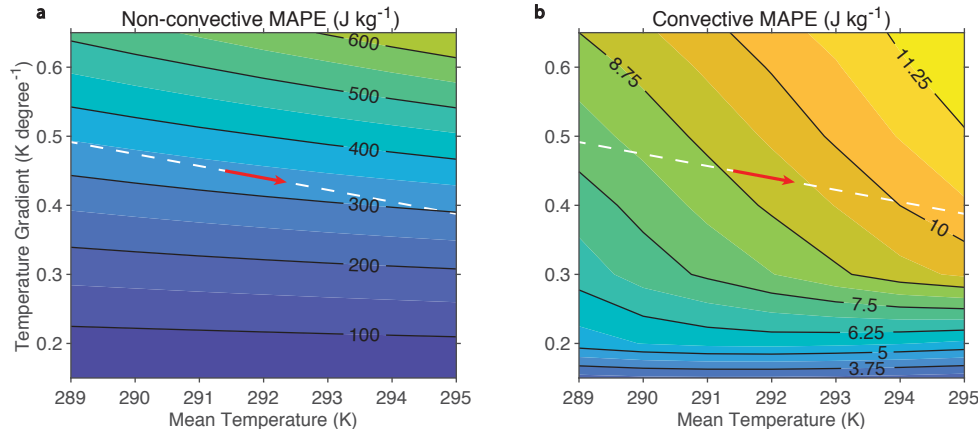
526 **Figure 2:** Visualization of MAPE calculations. Parcel rearrangements in the calculation of (a)  
 527 moist MAPE and (b) non-convective MAPE based on climatological JJA zonal-mean  
 528 temperatures and relative humidities from the ERA-Interim reanalysis (1979-2017). Black  
 529 contours (contour interval 100hPa) show the pressure of a given air parcel in the minimum-enthalpy state, referred to as the reference pressure. Arrows schematically indicate vertical

530 motion of parcels. The red lines show where the reference pressure is equal to the pressure.  
 531 Blue shading in (a) indicates a region of lower-tropospheric air bounded by a discontinuity in  
 532 the reference pressure distribution, whose ascent to the upper troposphere corresponds to the  
 533 release of convective instability.



534

535 **Figure 3:** Time series and trends of energetic reservoirs for summer in the Northern  
 536 extratropics. (a) Percent anomaly from climatological (1979-2017) mean for non-convective  
 537 MAPE (blue line) and eddy kinetic energy (purple line), and (b) convective MAPE, which is  
 538 defined as the difference between moist MAPE and non-convective MAPE. All results shown are  
 539 for JJA over 20-80N based on ERA-Interim reanalysis. Trends and associated 90% confidence  
 540 intervals are given in each panel. The dashed black lines show the linear best-fit trends for (a)  
 541 non-convective MAPE and (b) convective MAPE.



542

543 **Figure 4:** Energetic reservoirs of idealized atmospheres. (a) Non-convective MAPE and (b)  
 544 convective MAPE in idealized atmospheres over the latitude band 20-80°N as a function of  
 545 mean surface temperature and mean surface meridional temperature gradient in that latitude  
 546 band. The idealized atmospheres are representative of Northern Hemisphere summer (see  
 547 Methods for details). Contour intervals are  $100 \text{ J kg}^{-1}$  in (a) and  $1.25 \text{ J kg}^{-1}$  in (b). Red arrows  
 548 indicate changes in the JJA atmosphere based on ERA-Interim trends over 1979-2017 (see Fig.  
 549 S7 and Methods for details), and white dashed line extends these changes along the same slope  
 550 for clarity.

551  
 552